Next Materials 7 (2025) 100444

Contents lists available at ScienceDirect

Next Materials

journal homepage: www.sciencedirect.com/journal/next-materials

Research article

Synthesis of biochar and its metal oxide composites and application on next sustainable electrodes for energy storage devices

Bruna Andressa Bregadiolli [a,1], Glauco Meireles Mascarenhas Morandi Lustosa [a], João Vitor Paulin [b], Waldir Antonio Bizzo [c], Lauro Tatsuo Kubota [d], Shuguang Deng [e], Talita Mazon [a,*]

[a] Centro de Tecnologia da Informação Renato Archer - CTI, Campinas, SP, Brazil
[b] Faculdade de Ciências, Departamento de Física e Meteorologia, Universidade Estadual Paulista (UNESP), Bauru, SP, Brazil
[c] Faculdade de Engenharia Mecânica, Universidade Estadual de Campinas, Campinas, SP, Brazil
[d] Instituto de Química, Universidade Estadual de Campinas, Campinas, SP, Brazil
[e] School for Engineering of Matter, Transport & Energy - Arizona State University, Tempe, AZ, United States

ARTICLE INFO

Keywords:
Sugarcane biomass
Biochar
Hydrothermal synthesis
Supercapacitor

ABSTRACT

Biochar materials have been applied in energy storage due to their unique properties, such as high storage of ions, high conductivity, chemical stability and ease of production. Combining it with the high specific capacitance could be a promising strategy to develop devices and improve the properties. Through a hydrothermal technique the biochar powders were synthesized from sugarcane biomass. An acid pretreatment was carried out before and after the graphitization process aiming to obtain carbon materials with high surface area and porosity. The morphological characterization reveals powders with pores of submicrometer diameter. For the pure biochar it was determined a superficial area of 477.66 $m^2.g^{-1}$ with a median pore size of 42.92 Å and a pore volume of 0.21 $cm^3.g^{-1}$. A carbon-based paste was then prepared to deposit on nickel foam and obtain the electrodes. In a 3-electrode system characterization, biochar has showed higher specific capacitance than the metal oxide composites due to higher surface area and higher medium pore diameter. It was calculated a resistance of 2.7 Ω, a capacitance of 446 $mF.g^{-1}$, a power density of 46.2 $W.kg^{-1}$ and an energy density of 1.8 $W.h.kg^{-1}$. These results indicate the potential use of biochar-based electrodes with high electrical conductivity and improved surface area to obtain higher capacitance properties for development of advanced devices.

1. Introduction

As global energy consumption rises and the push for sustainability intensifies, developing new and efficient energy storage solutions becomes a critical challenge for scientists. The need is diverse, ranging from powering portable electronics and electric vehicles to supporting large-scale power plants and integrating renewable energy sources into our grids. Each application demands storage systems with specific characteristics for optimal performance. While technologies like batteries, hydrogen storage, superconducting magnets, and supercapacitors exist, finding a single ideal solution that meets all technical and economic needs remains elusive. [1–5]

The so-called supercapacitors are a class of energy storage devices that combine the properties of batteries, such as high storage capacity, with those of capacitors, such as ultra-fast charging and power supply, tolerating a large number of charge cycles [6,7]. However, these devices still have some drawbacks: the energy storage capacity is even less than that of conventional batteries, the observed voltage discharge curve can prevent the use of all stored energy and also an excessive self-discharge is observed.

The search for supercapacitor materials has spurred the development of numerous strategies, since its structure is essential for the performance of the supercapacitor to improve the characteristics as power density, charging time and cyclability [8]. A leading approach involves crafting novel functional composites with properties meticulously tailored to specific applications. These composites are created by merging two or more materials, each possessing unique properties, to achieve a synergistic effect. For instance, the combination of metal

---

* Corresponding author.
E-mail addresses: bruna@tsmc.com (B.A. Bregadiolli), talita.mazon@cti.gov.br (T. Mazon).

[1] Present address: 5088 W Innovation Cir, Phoneix AZ 85083.

https://doi.org/10.1016/j.nxmate.2024.100444
Received 31 July 2024; Received in revised form 26 November 2024; Accepted 26 November 2024

oxides and carbon-based materials has shown promise in various applications, including photocatalysis, sensors, and most notably, energy storage and transport. [9–13]

Among the metal oxides, the zinc oxide and copper oxides are attracting significant interest as electrode materials due to their versatility and combination of desirable properties. Zinc oxide (ZnO) has a wide band gap (3.37 eV), exceptional chemical stability, strong exciton binding energy at room temperature and piezoelectric properties that make it valuable in sensors. ZnO's advantages extend beyond its properties; it boasts easy and cost-effective manufacturing, environmental friendliness, and abundance, making it a sustainable choice. These attributes have propelled ZnO to the forefront of various applications in electronics, photocatalysis, and sensors. More recently, researchers are exploring its potential to enhance the stability of supercapacitors [14–21]. Likewise, CuO and CuO_2 materials are abundant, inexpensive, non-toxic, and readily synthesized in various nanostructures, all of which are crucial factors for practical applications, since they boast high capacities for storing lithium ions. However, fewer studies have investigated the application of CuO as a supercapacitor [22–25].

Carbonaceous materials, including graphite, graphene, and amorphous carbon, have been applied as electrodes for supercapacitors due to posses good electrical conductivity, ability to be functionalized and low reactivity [26,27]. However, non-renewable sources were used extensively to produce activated carbon (AC). This stands in contrast to the increasing public concern about climate change, environmental pollution and its health impacts. Recent advancements in material synthesis offer a promising solution to environmental concerns, such the development of methods to use biomass, organic plant matter, for the production of biochar, a type of AC. Biomass derivatives have presented outstanding electrochemical performance because it has high porosity, high surface area, chemical stability and electronic conductivity [7,28].

Employing a sustainable combination of physical and chemical techniques to reuse and convert biomass wastes to production of biochar not only represents cost-effective and easily scalable process, but also yields a highly porous material with a vast surface area [7,29]. In addition, the use of biochar offers others advantages for the environment: it replaces fossil fuels, reduces waste and captures carbon. These remarkable qualities position biochar as a promising candidate for energy storage applications [30–34]. Different biomass sources can be used as raw material, such as sugarcane, bamboo, cotton, coconuts sheel, banana, celtuce or even funghi [28,35–40] and have been used as cathode in supercapacitors with excellent results. However, the carbon-based energy density represents an important key to overcome and unlock the potential of this material in the application of energy storage.

Despite its promise, these materials can suffer from limitations, particularly the breakdown of its crystalline structure during repeated charging and discharging cycles (ion insertion and extraction). Synthesis approaches, including controlled nanostructuring, are being actively explored to address these limitations and then enhance the stability of the metal oxide@carbon electrodes, leading to an improved on performance, ciclability and life time [41]. Green carbon materials and their composites are rapidly emerging as game-changers in materials science. In response to growing environmental and engineering concerns, research efforts in materials science have intensified, leading to the development of promising new materials.

Here, in this work, we focus on development methodology for synthesis and characterization of carbon-based materials derived from sugarcane through pyrolysis followed by acidic and hydrothermal treatments, resulting in a graphitized structure: porous biochar and composites containing copper oxide (CuO) or zinc oxide (ZnO). We employed a unique yet efficient approach to grow nanoparticles from these metal oxides directly onto the biochar surface. This method involves a pre-deposition step to create a "seed layer" – a technique commonly used for thin films. This seed layer promotes the nucleation and controlled growth of the desired metal oxide on the biochar. We investigated the morphology and oxide growth patterns on the biochar surface using various characterization techniques and then the preparation of electrodes on nickel foam to verify the potential use in energy storage applications.

2. Experimental procedure

2.1. Raw materials

Natural sugarcane (*Saccharum officinarum*) bagasse was obtained from plantations in the region of Campinas/SP-Brazil. Sulfuric acid – H_2SO_4, phosphoric acid – H_3PO_4, ammonium hydroxide – NH_4OH, zinc acetate – $Zn(CH_3COO)_2$, zinc nitrate – $Zn(NO_3)_2.6H_2O$, copper acetate – $Cu(CH_3COO)_2$, copper nitrate – $Cu(NO_3)_2.3H_2O$, carbon nanotubes single-walled, poly(vinylidene fluoride) – PVDF, *N*-methyl-2-pyrrolidone – NMP. All the chemicals were purchased from Sigma-Aldrich with analytical purity grade.

2.2. Synthesis of biochar powders

Initially the crude sugarcane bagasse biomass (5 g) was pre-treated in an acidic solution (100 mL H_2O, 15 mL H_2SO_4, and 15 mL H_3PO_4) during 2 hours. Then, it was transferred into a Teflon vessel (PTFE), accommodated in a stainless-steel reactor, and hydrothermally treated (80̊C, 2 h). After cooling down, the solution was filtered and washed until neutral pH. Next, the product was overnight dried in the oven and thermally treated (750̊C, 7 h in N_2 atmosphere). The carbon product (namely biochar) was recovered and sieved in a 200-mesh sieve and then stored in hermetically sealed bottles to later be used to prepare the electrodes.

To obtain the biochar composites with metal oxide, firstly its necessary prepare a seed layer by mixing 0.5 mg of the biochar dispersed in ethanol with addition of the respective acetate ($Zn(CH_3COO)_2$ or $Cu(CH_3COO)_2$ - 80 mM) at room temperature (25°C) for 2 hours. To promote the oxide growth on the biochar surface, the mixture was added to a Teflon container with deionized water (200 mL) and ammonium hydroxide (NH_4OH - 6.5 mL), in an oil bath at 90̊C/2 h, using the respective nitrate as precursor agent (1.7824 g of $Zn(NO_3)_2.6H_2O$ or 1.4496 g of $Cu(NO_3)_2.3H_2O$).

Finally, the solution was centrifuged at 10,000 rpm for 30 min and the obtained powder was overnight dried at 100̊C. No further sintering process of the powders was performed. A pure biochar was also synthesized in order to compare and verify the influence of oxides in the properties.

2.3. Electrode preparation

A paste was prepared by mixing ~20 mg of biochar with polyvinylidene fluoride (PVDF) (5 %), carbon nanotubes (5 %) and addition of ~2 drops of *N*-methyl-2-pyrrolidone (NMP). After homogenization, the paste was dropped on a nickel foam electrode (1×1 cm) followed by drying at 60 °C for 24 hours.

2.4. Characterizations

To evaluate the size and shape of the carbonized powders and oxide nanoparticles the Scanning Electronic Microscopy (SEM) was performed by from Tescan model Mira 3 XMU operated at an acceleration voltage of 15 kV.

N_2 physisorption/desorption isotherms were recorded at 77 K using a Micromeritics 3-Flex instrument. Before analysis, all samples were outgassed under a secondary vacuum for 12 h at 623 K. Surface areas were obtained by applying the Brunauer–Emmett–Teller (BET) equation to the linear zone of the BET plot ($P/P_0 = 0.01–0.3$). Pore size distribution and pore volume are determined by the Barrett-Joyner-Halenda (BJH) method.

X-Ray Diffraction (XRD) were conducted in a range of $2\theta = 10$–80° with increment of $\Delta 2\theta = 0.02^\circ$ (CuKα radiation, $\lambda = 1.5460$ Å using CuKα radiation ($\lambda = 1.5418$ Å) performed by XRD7000 Shimadzu X-ray diffractometer.

Raman Spectroscopy measurements were conducted in a Horiba Jobin Yvon Spectrometer, model T64000, in a spectral range of 100–3500 cm^{-1} (5 scans) and using a 532 nm laser.

Electrochemical characterizations were performed using a three-electrode system at a Potentiostat AutoLab (PGSTAT302N model) electrochemical workstation. Silver/silver chloride (Ag/AgCl) and platinum (Pt) wire were used as the reference electrode and counter electrode, respectively. The nickel foam electrode was used as the working electrode. 1 M Na_2SO_4 was used as neutral aqueous electrolyte, due to easy handling and strong solvation behavior of SO_4^{-2} ions [42]. Cyclic Voltammetry (CV) was performed within the range of −0.2–0.6 V at 10, 50, 100 and 200 $mV.s^{-1}$ scan rates. Galvanostatic Charge-Discharge (GCD) was performed at a current density of 0.1 $A.g^{-1}$. Impedance Spectroscopy (IS) was recorded using voltage amplitude of 100 mV at frequencies ranging from 100 to 0.1 Hz and 200 mV offset DC voltage.

3. Results and discussion

3.1. Morphological and structural characterizations

The as-synthesized biochar based powders were characterized regarding their specific surface area by the N_2 adsorption method (S_{BET}) based on the determination of monolayers of gas adsorbed on the particles that make up the analyzed material. The method provides information on the specific surface area based on the volume of gas used in N_2 adsorption-desorption phenomena. From the obtained isotherms showed in Fig. S1-S3, it was possible to determine the pore size distribution and specific surface area, calculated by the Brunauer-Emmett-Teller (BET) method. The results were shown in Table 1. The biochar had a surface area of 477.66 $m^2.g^{-1}$ with a median pore size of 42.915 Å and a pore volume of 0.21147 $cm^3.g^{-1}$. After the oxide growth, the surface area decreases to 152.48 $m^2.g^{-1}$ for CuO@biochar and 163.68 $m^2.g^{-1}$ for ZnO@biochar. By comparing the porous diameter, no significant change is observed for CuO@biochar (42.963 Å). However, a smaller porous diameter, 21.177 Å, is obtained for ZnO@biochar due to smaller nanorods partially filling the porous during the growth. The pore volume also decreased after oxide growth. The presence of porous allows a better electrolyte penetration, which will lead to more electrochemical active sites, and it is beneficial for their capacitive performance. Despite the reduction in porosity, the formation of semiconductor oxide nanostructures can create preferential pathways for ion diffusion. These structures may present defects that act as channels for ion migration, thus acting as ion adsorption sites and facilitating their retention and subsequent transport.

The morphologies of the as-synthesized powders were analyzed by SEM and showed in Fig. 1a,b for pure biochar, in Fig. 1c,d for ZnO@biochar and in Fig. 1e,f for CuO@biochar. Through the images it was verified that the pure biochar showed particles with irregular plates shapes with different sizes and thickness; it also observed pores in the carbon structures. From the micrographs of the biochar based powders, and using the ImageJ software to determine sizes of the as-synthesized nanostructures, it was observed a good covering on carbon surfaces with longitudinal growth of ZnO as nanorods (NR) with diameter size in a range of 40 – 60 nm and the CuO showed a planar growth as nanosheets (NS) with a thickness size of ~25 nm and a length size in a range of 60 – 130 nm. These oxides nanostructures may have grown into the pore region, leading to a decrease in surface area (as seen in Table 1), but at the same time they can promote good permeation of the ions from the electrolyte.

Table 1
Pore diameter, BET surface area and pore volume of biochar based powders.

Sample	Pore Diameter (Å)	BET Surface Area ($m^2.g^{-1}$)	Pore Volume ($cm^3.g^{-1}$)
Pure Biochar	42.915	477.66	0.21147
ZnO@biochar	21.177	163.69	0.00724
CuO@biochar	42.963	152.48	0.06755

X-ray diffraction (Fig. 2) made it possible to identify the crystalline phase from the nanostructures grown on the surface of the biochar. The well-defined intense peaks provide strong evidence for the formation of highly crystalline oxides. The obtained peaks from Fig. 2a were indexed to the ZnO hexagonal wurtzite structure, according to JCPDS Card nº 36–1451 [43], and in Fig. 2b, the peaks can be indexed to the CuO monoclinic structure, according to JCPDS Card nº 01–080–0076 [44]. For both biochar composites, it also observed a broad peak in the region of 25–30°, which is typically assigned to the C<002> diffraction peak related to amorphous carbon (JCPDS 41–1487 [45]), indicating the presence of randomly oriented aromatic sheets within the biochar component.

Raman Spectroscopy was used to analyze the graphitization degree and defects of the material. The spectrum of the pure biochar (Fig. 3a) shows the characteristics regions of carbon-graphene-like at 1340 cm^{-1} (D-band) and at 1590 cm^{-1} (G-band). The D-band can be associated with defect sites or disordered sp^2-hybridized carbon atoms and can provide information about the number of layers [46]. The G-band is associated to the first order scattering of the $E_{2\,g}$ phonon of symmetric stretching of C-C bond with sp^2 hybridization. From intensity ratio determination of the D-band and G-band (I_D/I_G) it was possible obtain information about carbon materials disorder degree and graphitization [47]. The I_D/I_G of the biochar was 0.96 (which means a high degree of graphitization), and for the composite powders were calculated an I_D/I_G of 0.91 for ZnO@biochar and 1.04 for CuO@biochar. Comparing to pure biochar, the lower ratio for ZnO@biochar signifies a more ordered and defect-free structure and the high value for CuO@biochar indicates a higher concentration of defects and disorder within the carbon-based powder sample [46].

In the spectrum of ZnO@biochar, shown in Fig. 3b, it were identified the spectroscopic peaks that assigned to a hexagonal wurtzite ZnO structure at 200, 330, 430, 570, and 650 cm^{-1}, in accordance to the literature [48]. The graphitized biochar D- and G-bands at 1340 and 1595 cm^{-1}, respectively, are also observed. Among the Raman peaks, the E_2 vibration mode centered at 430 cm^{-1} has a stronger intensity and narrower line width, which is the characteristic of wurtzite hexagonal phase and showed good crystalline quality [48,49]. The Raman spectra of CuO@biochar, shown in Fig. 3c, with the prominent peaks at 285, 335, and 615 cm^{-1}, corresponding to first-order Raman-active mode of A_g, $B_{1\,g}$, and $B_{2\,g}$ symmetries, attributed to the movement of oxygen atoms in the b-direction, and perpendicular to the *b*-axis of the monoclinic CuO structure, respectively [50].

For each Raman spectra the region of 1200 – 1700 cm^{-1} was selected, normalized and then fitted with two Lorentzian peaks to analyze the characteristic of the D- and G-bands. The results of peak fitting analysis are reported in Table 2. The slightly deviations in the D-peak could also be expected due to some interference from oxide nanoparticles. The decrease in G-peak position indicates a decrease in sp^2 clustering due to greater cross of π-states in biochar. The higher values of D-peak width indicates an decrease in the disordered structure of the six-fold rings, suggests the presence of a larger number of sp^2 clusters of different sizes and orders, while the increase of the G-peak width indicates an increased bond angle disorder in the sp^2 distorted rings. The integrated intensity ratio of D-to G-peak (A_D/A_G) closer to and greater than 2 indicates the well-defined porous structure of the activated carbon, as observed for pure biochar. In comparison of ZnO@biochar ($A_D/A_G = 4.4$) to CuO@biochar ($A_D/A_G = 7.2$) a ratio exceeding 7 signifies an extremely high concentration of defects and a minimal presence of ordered sp^2 bonding within the powder sample. [51–54]

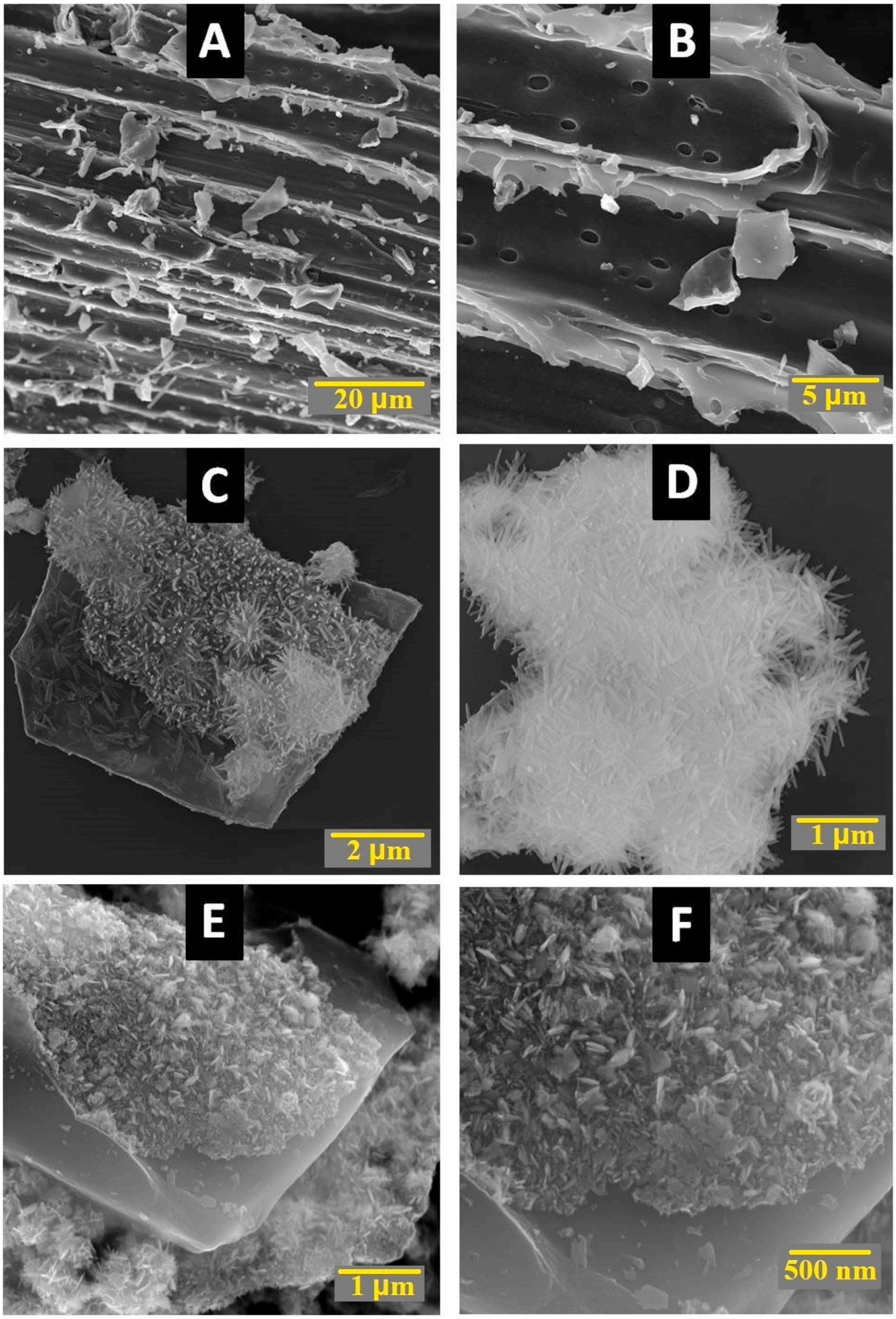

Fig. 1. SEM images of (a,b) pure biochar, (c,d) ZnO@biochar and (e,f) CuO@biochar. Different magnifications.

3.2. *Electrochemical performance*

The electrochemical behavior and potential for energy storage of the biochar based systems were characterized at room temperature and in a three-electrode system using a 1 M Na_2SO_4 aqueous solution as electrolyte through Impedance Spectroscopy (IS), Cyclic Voltammetry (CV) and Galvanostatic Charge-Discharge (GCD).

Fig. 4a-c shows the CV curves of the biochar, ZnO@biochar, and CuO@biochar samples at different scan rates in a range of 10–200 mV.s^{-1}. All as-prepared biochar-based electrodes exhibited a characteristic quasi-rectangular shape with an increase of the cyclic loop area as the scan rate was raised, indicating that the system is accumulating charge. Even at lower scan rates (10 mV.s^{-1}) the quasi-rectangular behavior of the curves were observed for the electrodes [55]. The no observance of distinct oxidation and reduction peaks suggests that these electrodes store energy via pseudocapacitance, i.e., the storage mechanism involving ion adsorption and desorption. From the CV curves it was possible determine the specific capacitance according to Eq. 1 [20]. Through this formula and using the CV curve at 200 mV.s^{-1}, it was determined a capacitance of 446 mF.g^{-1} for pure biochar, 84 mF.g^{-1} for ZnO@biochar and 44 mF.g^{-1} for CuO@biochar. These findings can be associated with the surface area values from Table 1.

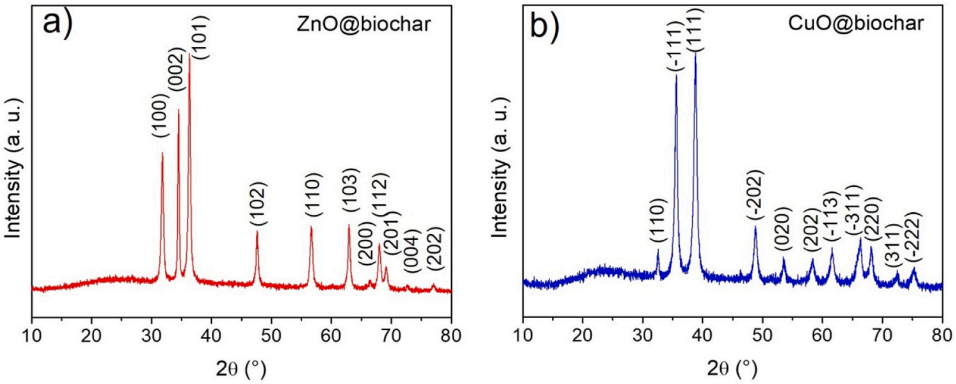

Fig. 2. XRD patterns of (a) ZnO@biochar and (b) CuO@biochar.

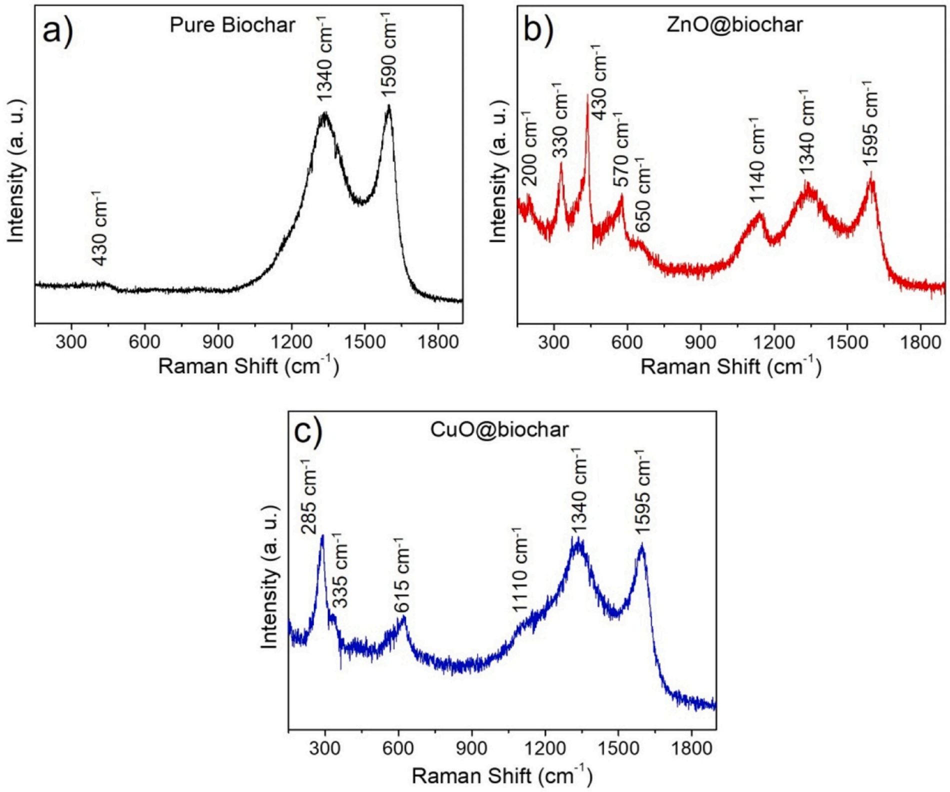

Fig. 3. Raman spectrum for (a) pure biochar, (b) ZnO@biochar and (c) CuO@biochar.

Table 2
Peak parameters of biochar based powders.

Peak Parameter		Pure Biochar	ZnO@biochar	CuO@biochar
D-band (~1360 cm^{-1})	Position (cm^{-1})	1339.97	1337.92	1332.68
	Width (cm^{-1})	277.81	369.81	439.11
G-band (~1580 cm^{-1})	Position (cm^{-1})	1595.81	1594.48	1593.93
	Width (cm^{-1})	82.47	108.77	85.82
Ratios	I_D/I_G	0.96	0.91	1.04
	A_D/A_G	3.79	4.40	7.21

$$C_S = \int_{V_2}^{V_1} I(V)dV \Big/ m\nu(\Delta V) \tag{1}$$

where: $\int_{V_2}^{V_1} I(V)dV$ is the integral areas of the cyclic voltammetry loop, m is the mass of the biochar material deposited in g, ν is the scan rate in V/s and ΔV represent the potential window size in V. C_S is the specific capacitance in F/g.

The GCD measurements were also carried out to evaluate the electrochemical characteristics. The results, shown in Fig. 4d, were obtained at density current of 0.1 $mA.g^{-1}$. All materials have shown a similar symmetrical triangular curve, with the biochar suggesting a longer discharge time (about four times). However, ZnO@biochar has presented a higher potential than biochar and CuO@biochar, as would be expected based on the low electrical conductivity and cyclability of CuO [25]. From CDG curves, it is also possible to obtain the IR Drop, i.e., a voltage drop that arises from the inherent resistance of the biochar

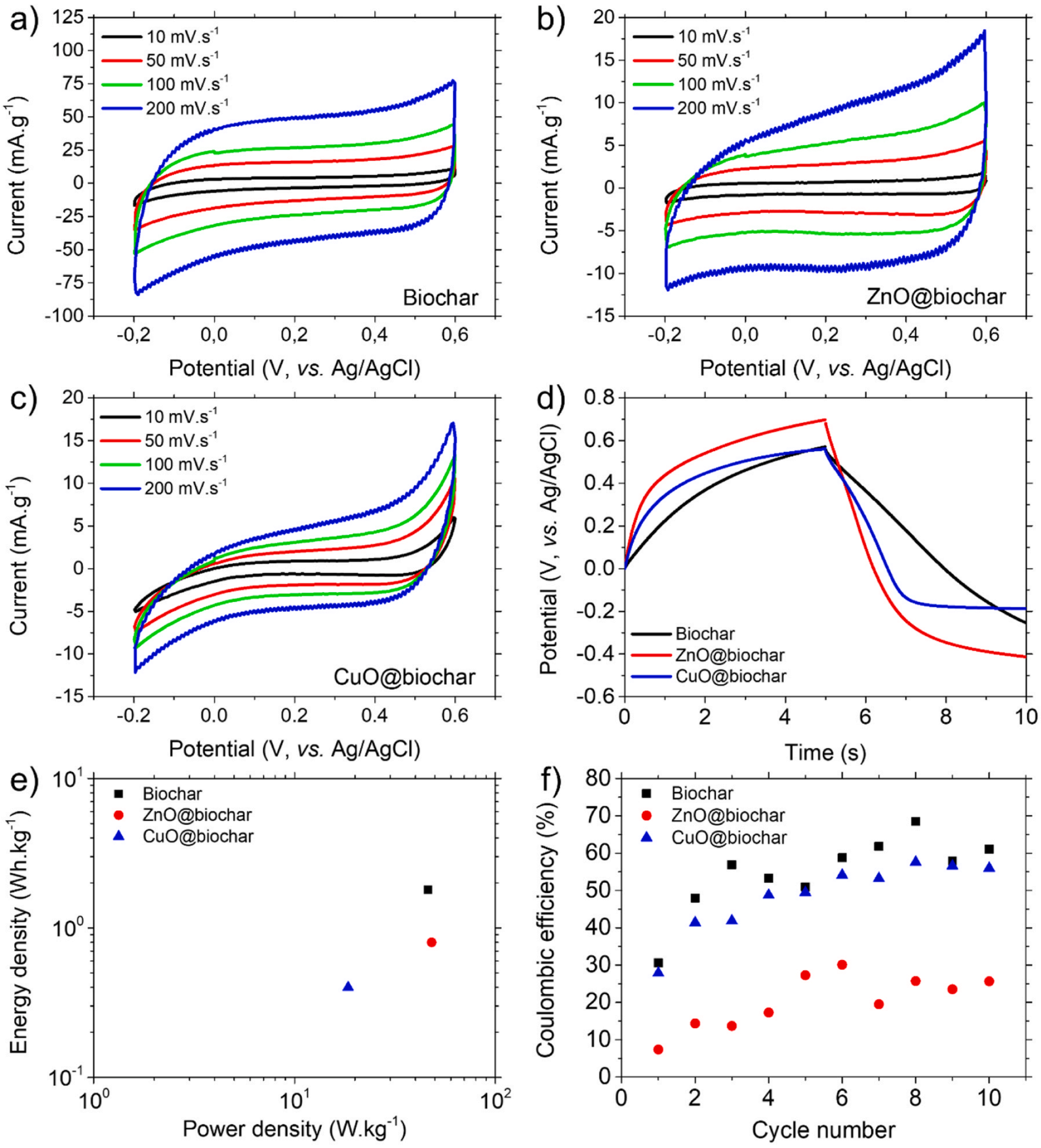

Fig. 4. Cyclic Voltammetry of (a) biochar, (b) ZnO@biochar and (c) CuO@biochar at different scan rates. (d) GCD curves and (e) Ragone plot for biochar based powders. (f) Coulombic efficiency as a function of cycle number for biochar and oxides@biochar.

electrode material and the electrical contacts within the device. It can affect the overall performance of the capacitor. All biochar-based electrodes showed low IR drop values: 0.014 V for Biochar, 0.012 V for Cu@biochar, and 0.0165 V for ZnO@biochar. Based on these profiles, two performance metrics, known as power density and energy density, were deduced, as they are the most relevant parameters for applications. The energy density (E – W.h.kg^{-1}) represents the amount of storage or deliverable electrical energy and can be determined by Eq. 2. On the other hand, the power density (P – W.kg^{-1}) determines the efficiency in energy uptake/delivery and is estimated by Eq. 3. [56–58]

$$E = C_s \Delta V^2 / 2 * 3.6 \tag{2}$$

$$P = E * 3600 / \Delta t_{dis} \tag{3}$$

where Δt_{dis} is the discharge time, ΔV is the cell voltage.

The power density of the electrodes was estimated as being 46.2 W.kg^{-1} for the pure biochar, 48.2 W.kg^{-1} for the ZnO@biochar and 18.5 W.kg^{-1} for the CuO@biochar, and the energy density was 1.8, 0.8 e 0.4 Wh.kg^{-1}, for the materials in the same order. Based on these data, the Ragone plot [56] was outlined and is shown in Fig. 4e. As can be seen, biochar performs better than the composites. Furthermore, the cycle performance was considered by consecutive GCD tests and analyzed by the coulombic efficiency [59], according to Eq. 4. This parameter provides information to evaluate the cycle stability of electrode by comparing the first and the end cycle.

$$\eta = \left(t_D / t_C \right) \times 100\% \tag{4}$$

where t_D and t_C are the discharge and charge times in second.

In all cases, according to Fig. 4 f, the coulombic efficiency increases after the first cycle. This behavior can be attributed to the materials porous structure, by which in the first cycle a higher concentration of electrolyte ions was adsorbed than desorption. Later, the stability could be understood as a smooth adsorption and desorption during each charging and discharging cycle. [56]

To optimize supercapacitor performance, understanding the underlying charge storage mechanisms is crucial. Hybrid materials often exhibit a combination of two primary storage mechanisms: (i) Electric Double-Layer Capacitance (EDLC), the mechanism involves the adsorption and desorption of electrolyte ions at the electrode-electrolyte interface, forming an electric double layer, and (ii) Pseudocapacitance, the mechanism relies on fast and reversible redox reactions occurring at the electrode surface or within its bulk. The Dunn method was employed to determine and differentiate the capacitive and diffusive contributions of the as-prepared electrodes from the CV curves, utilizing Eqs. 5 and 6 [60–63]. As illustrated in Fig. 5, the diffusion-controlled process dominates the charge storage mechanism at lower scan rates. However, as the scan rate increases, a significant contribution from the capacitive process becomes evident. This transition from diffusion-controlled to capacitive-controlled behavior is attributed to the increased contribution of surface-controlled reactions at higher scan rates. These findings suggest that the developed electrode material exhibits a hybrid behavior, combining both diffusion-controlled and capacitive-controlled mechanisms, which can lead to enhanced electrochemical performance.

$$i(\nu) = k_1\nu + k_2\nu^{1/2} \tag{5}$$

$$\frac{i(\nu)}{\nu^{1/2}} = k_1\nu^{1/2} + k_2 \tag{6}$$

where $k_1\nu$ is the capacitive on-contrary, $k_2\nu^{1/2}$ shows the diffusive contributions in the total current $i(\nu)$ of the working electrode. The values of constants k_1 and k_2 will be measured from the intercept and slope of the graph $\frac{i(\nu)}{\nu^{1/2}}$ vs $\nu^{1/2}$.

The electrochemical behavior of the electrode/electrolyte interface was investigated through electrochemical impedance spectroscopy (EIS) to clarify the supercapacitor's potential charge storage mechanism. Fig. 6a shows the Nyquist plots of the biochar and composites in the frequency range of 100 kHz to 0.1 Hz with 200 mV of DC bias. As can be seen, the spectra show a similar shape with an incomplete semicircle at high frequency and a linear tail at the low-frequency region but with different intensities, indicating the pseudocapacitive effects. The Nyquist plots were modeled by the equivalent circuit reported in Fig. 6b and the fitting parameters are shown in Table 3. This circuit exhibit four different elements, namely uncompensated resistance (R_u), charge-transfer resistance (R_{CT}), constant phase element (Q_{CPE}) and Warburg element (W) [64–67]. R_u represents the ionic resistance of the electrolyte in combination with the electronic resistance of the electrodes, which implies that biochar has a better injection into the electrode as it is about two times lower than the composites. This behavior is also compatible with biochar's lower electron-transfer processes kinetics between the electrode-electrolyte, represented by the R_{CT}, compared to the ZnO@biochar and CuO@biochar composites.

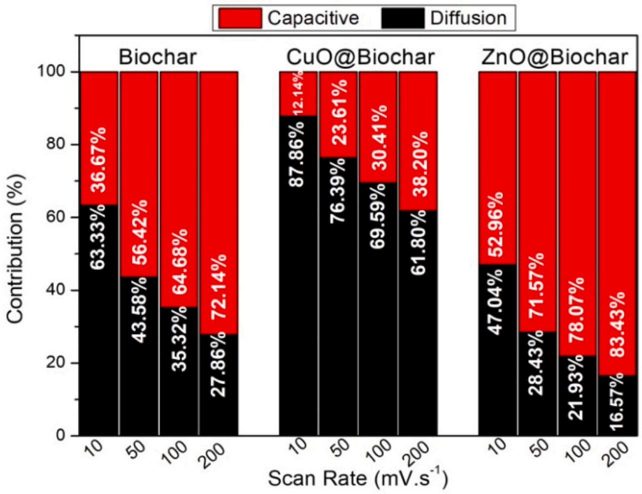

Fig. 5. Percentage of contribution from diffusion and capacitive process in charge storage of biochar-based composite electrodes.

As suggested by the Nyquist shape, the pseudocapacitive processes originate a capacitive response that deviates the system from an ideal capacitor [64,65,68]. A pure capacitor is obtained when $n = 1$ at the Q_{CPE} impedance (Z_Q) given by Eq. 7:

$$Z_Q = Q^{-1}/(j.\omega)^n \tag{7}$$

where j is a unitary unit and ω is the angular frequency.

In this case, for the pure biochar it was achieved a $n = 0.70$ and for both composites a $n = 0.8$. Such behavior indicates that the composites behave more like a capacitor than the biochar. When we analyze the phase angle dependence on the frequency, as shown in Fig. 5c, this trend is observed at frequencies around 50 Hz. However, at low frequencies, dominated by ionic processes, the biochar and ZnO@biochar have a slightly improved capacitance behavior. Nonetheless, from the graph of capacitance as a function of frequency, according to the Eq. 8, it is possible to observe in Fig. 6d that the biochar capacitance is about one order in magnitude to both composites, with a similar frequency-dependent feature.

$$C(f) = -1/(\omega Z\prime) \tag{8}$$

A further assessment of Fig. 6c indicates that the corresponding relaxation time constant τ_0 (obtained at the 45° phase angle or the system's characteristic frequency) 51.53 is 3.5 ms for pure biochar, 2.0 ms for ZnO@biochar, and 1.1 ms for CuO@biochar. The higher relaxation time constant suggests slow ion diffusion and transport behavior or higher ionic diffusion pathways, similar to the BET surface area. The Warburg ohmic resistance (W_O-R, Table 3) being higher for the biochar and comparable for the composites is also compatible with the above proposition. Therefore, we speculate that the better energy storage capability of biochar is due to its higher porosity that enables the occurrence of multiple-electron transfer reactions in the material. [68, 69]

4. Conclusion

Composites based on biochar derivate from sugarcane with oxides on the surface were synthesized through a facile and scalable synthetic procedure. By using the hydrothermal synthesis it was possible to produce nanostructures directly onto the carbon surface. The structural, morphological and electrochemical characterizations of biochar based electrodes were investigated and compared. Biochar was successfully synthesized with high surface area and porous structure, showing a better capacitive behavior than the metal oxide biochar composites. From the applied methodology it can be inferred that all the biochar here synthesized shows potential to be applied in development of energy storage devices. These results indicate that is more important develop a route synthesis to improve surface area and promote a porous structures than combining graphitized biochar with metal oxides. The utilization of sugarcane bagasse as the biochar precursor offers a sustainable and cost-effective approach compared to traditional materials like activated carbon, in addition with the possibility of large-scale biochar production. This reduces reliance on environmentally harmful processes and expensive raw materials. The electrical performance of the as-prepared biochar electrode opens exciting possibilities for further research and development in advanced carbon-based materials for energy storage applications.

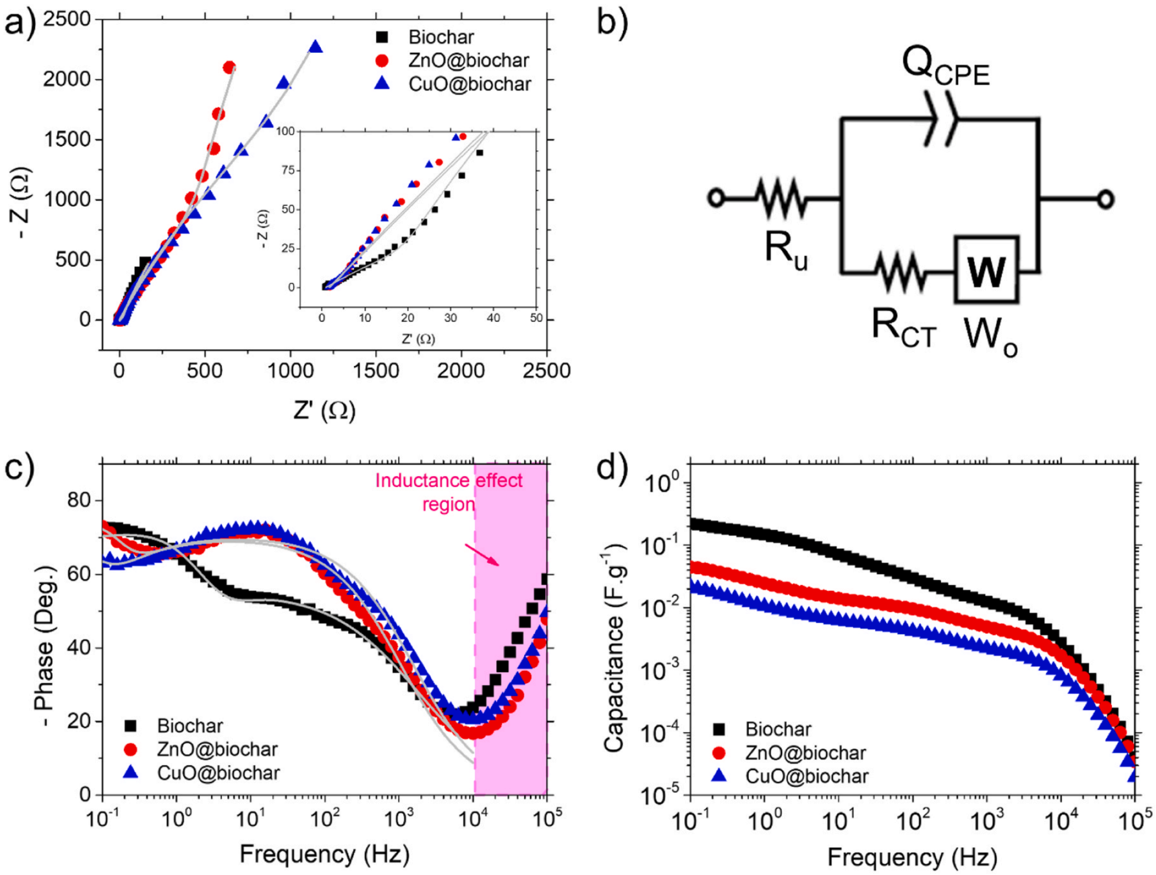

Fig. 6. (a) Nyquist plot biochar based powders and (b) correspondent equivalent circuit model. Graphs of (c) angle phase *vs.* frequency and (d) frequency-capacitance.

Table 3
Fitting parameters for equivalent circuits and Nyquist plots.

Element	Pure Biochar	ZnO@biochar	CuO@biochar
R_u (Ω)	0.74	1.77	1.55
Q ($m\Omega^{-1}$)	1.95	0.57	0.46
n (unitless)	0.70	0.78	0.79
R_{CT} (Ω)	2.70	7962.00	8988.00
W_O-R (Ω)	136.80	1.15	1.74
W_O-T (ms)	135.77	0.65	0.62
W_O-P (unitless)	0.49	0.62	0.52

*The Warburg diffusion element is divided into three components: W_O-R represents the diffusion impedance, W_O-T is the system diffusion time and W_O-P is an exponential factor.

Funding

Research supported by CTI-Nano, strategic laboratory from SisNano, MCTI and financed by CNPq (301120/2021-8). State of São Paulo Research Foundation (FAPESP, grants: CEPID-CDMF 2013/07296-2, 2018/04487-5). J.V.P. also acknowledges the FAPESP support (grant: 2020/15869-6).

CRediT authorship contribution statement

Bruna Andressa Bregadiolli: Formal analysis, Methodology, Investigation, Writing - Original Draft, Visualization. **Glauco Meireles Mascarenhas Morandi Lustosa:** Formal analysis, Writing - Original Draft, Visualization. **João Vitor Pauli:** Formal analysis, Investigation. **Waldir Antonio Bizzo:** Conceptualization, Methodology, Visualization, Supervision. **Lauro Tatsuo Kubota:** Conceptualization, Methodology, Visualization, Supervision. **Shuguang Deng:** Conceptualization, Visualization. **Talita Mazon:** Conceptualization, Methodology, Visualization, Supervision, Project administration, Funding acquisition.

Declaration of Competing Interest

The authors declare the following financial interests/personal relationships which may be considered as potential competing interests: Talita Mazon reports financial support was provided by National Council for Scientific and Technological Development. Talita Mazon reports financial support was provided by State of Sao Paulo Research Foundation. Joao Vitor Paulin reports financial support was provided by State of Sao Paulo Research Foundation. Glauco Meireles Mascarenhas Morandi Lustosa reports financial support was provided by National Council for Scientific and Technological Development. If there are other authors, they declare that they have no known competing financial interests or personal relationships that could have appeared to influence the work reported in this paper.

Appendix A. Supporting information

Supplementary data associated with this article can be found in the online version at doi:10.1016/j.nxmate.2024.100444.

Data availability

The datasets generated during the current study are available from the corresponding author on reasonable request.

References

[1] M. Conte, Supercapacitors technical requirements for new applications, Fuel Cells 10 (2010) 806–818, https://doi.org/10.1002/fuce.201000087.

[2] Z. Wang, Y. Wang, Q. Ding, C. Wang, K. Zhang, Energy storage economic analysis of multi-application scenarios in an electricity market: a case study of China, Sustain 12 (2020), https://doi.org/10.3390/su12208703.

[3] L. YAO, B. YANG, H. CUI, J. ZHUANG, J. YE, J. XUE, Challenges and progresses of energy storage technology and its application in power systems, J. Mod. Power Syst. Clean. Energy 4 (2016) 519–528, https://doi.org/10.1007/s40565-016-0248-x.

[4] A.T. Hoang, S. Nižetić, A.I. Olcer, H.C. Ong, W.-H. Chen, C.T. Chong, S. Thomas, S. A. Bandh, X.P. Nguyen, Impacts of COVID-19 pandemic on the global energy system and the shift progress to renewable energy: opportunities, challenges, and policy implications, Energy Policy 154 (2021) 112322, https://doi.org/10.1016/j.enpol.2021.112322.

[5] IEA, Global Energy Review 2021, Paris, 2021.

[6] J. Libich, J. Máca, J. Vondrák, O. Čech, M. Sedlaříková, Supercapacitors: properties and applications, J. Energy Storage 17 (2018) 224–227, https://doi.org/10.1016/j.est.2018.03.012.

[7] S. Saini, P. Chand, A. Joshi, Biomass derived carbon for supercapacitor applications: review, J. Energy Storage 39 (2021) 102646, https://doi.org/10.1016/j.est.2021.102646.

[8] S. Huang, X. Zhu, S. Sarkar, Y. Zhao, Challenges and opportunities for supercapacitors, APL Mater. 7 (2019) 100901, https://doi.org/10.1063/1.5116146.

[9] L. Hao, X. Li, L. Zhi, Carbonaceous electrode materials for supercapacitors, Adv. Mater. 25 (2013) 3899–3904, https://doi.org/10.1002/adma.201301204.

[10] A. Borenstein, O. Hanna, R. Attias, S. Luski, T. Brousse, D. Aurbach, Carbon-based composite materials for supercapacitor electrodes: a review, J. Mater. Chem. A. 5 (2017) 12653–12672, https://doi.org/10.1039/C7TA00863E.

[11] M. Zhi, C. Xiang, J. Li, M. Li, N. Wu, Nanostructured carbon–metal oxide composite electrodes for supercapacitors: a review, Nanoscale 5 (2013) 72–88, https://doi.org/10.1039/C2NR32040A.

[12] D. Sudha, P. Sivakumar, Review on the photocatalytic activity of various composite catalysts, Chem. Eng. Process. Process. Intensif. 97 (2015) 112–133, https://doi.org/10.1016/j.cep.2015.08.006.

[13] S. Torquato, S. Hyun, A. Donev, Multifunctional composites: optimizing microstructures for simultaneous transport of heat and electricity, Phys. Rev. Lett. 89 (2002) 266601, https://doi.org/10.1103/PhysRevLett.89.266601.

[14] K.S. Srikanth, A. Wazeer, P. Mathiyalagan, S. Vidya, K. Rajput, H.S. Kushwaha, 25 - Piezoelectric properties of ZnO. in: K.B.T.-N.Z.O. Awasthi (Ed.), Met. Oxides, Elsevier, 2021, pp. 717–736, https://doi.org/10.1016/B978-0-12-818900-9.00024-3.

[15] Ü. Özgür, Y.I. Alivov, C. Liu, A. Teke, M.A. Reshchikov, S. Doğan, V. Avrutin, S.-J. Cho, H. Morkoç, A comprehensive review of ZnO materials and devices, J. Appl. Phys. 98 (2005) 41301, https://doi.org/10.1063/1.1992666.

[16] M. Liangruksa, P. Sukpoonprom, A. Jankaew, W. Photaram, C. Siriwong, Gas sensing properties of palladium-modified zinc oxide nanofilms: a DFT study, Appl. Surf. Sci. 544 (2021) 148868, https://doi.org/10.1016/J.APSUSC.2020.148868.

[17] H. Kim, Y. Pak, Y. Jeong, W. Kim, J. Kim, G.Y. Jung, Amorphous Pd-assisted H2 detection of ZnO nanorod gas sensor with enhanced sensitivity and stability, Sens. Actuators, B Chem. 262 (2018) 460–468, https://doi.org/10.1016/j.snb.2018.02.025.

[18] E.H. Umukoro, M.G. Peleyeju, A.O. Idris, J.C. Ngila, N. Mabuba, L. Rhyman, P. Ramasami, O.A. Arotiba, Photoelectrocatalytic application of palladium decorated zinc oxide-expanded graphite electrode for the removal of 4-nitrophenol: experimental and computational studies, RSC Adv. 8 (2018) 10255–10266, https://doi.org/10.1039/c8ra00180d.

[19] L.S. Aravinda, K.K. Nagaraja, H.S. Nagaraja, K.U. Bhat, B.R. Bhat, ZnO/carbon nanotube nanocomposite for high energy density supercapacitors, Electrochim. Acta 95 (2013) 119–124, https://doi.org/10.1016/j.electacta.2013.02.027.

[20] Y. Zhang, X. Sun, L. Pan, H. Li, Z. Sun, C. Sun, B.K. Tay, Carbon nanotube–ZnO nanocomposite electrodes for supercapacitors, Solid State Ion. 180 (2009) 1525–1528, https://doi.org/10.1016/j.ssi.2009.10.001.

[21] X. He, J.E. Yoo, M.H. Lee, J. Bae, Morphology engineering of {ZnO} nanostructures for high performance supercapacitors: enhanced electrochemistry of {ZnO} nanocones compared to {ZnO} nanowires, Nanotechnology 28 (2017) 245402, https://doi.org/10.1088/1361-6528/aa6bca.

[22] V. Senthilkumar, Y.S. Kim, S. Chandrasekaran, B. Rajagopalan, E.J. Kim, J. S. Chung, Comparative supercapacitance performance of CuO nanostructures for energy storage device applications, RSC Adv. 5 (2015) 20545–20553, https://doi.org/10.1039/C5RA00035A.

[23] R. Kumar, P. Rai, A. Sharma, Facile synthesis of Cu2O microstructures and their morphology dependent electrochemical supercapacitor properties, RSC Adv. 6 (2016) 3815–3822, https://doi.org/10.1039/C5RA20331G.

[24] M. Yang, Q. Gao, Copper oxide and ordered mesoporous carbon composite with high performance using as anode material for lithium-ion battery, Microporous Mesoporous Mater. 143 (2011) 230–235, https://doi.org/10.1016/j.micromeso.2011.03.001.

[25] D.P. Dubal, D.S. Dhawale, R.R. Salunkhe, V.S. Jamdade, C.D. Lokhande, Fabrication of copper oxide multilayer nanosheets for supercapacitor application, J. Alloy. Compd. 492 (2010) 26–30, https://doi.org/10.1016/j.jallcom.2009.11.149.

[26] J.-S. Wei, T.-B. Song, P. Zhang, X.-Q. Niu, X.-B. Chen, H.-M. Xiong, A new generation of energy storage electrode materials constructed from carbon dots, Mater. Chem. Front. 4 (2020) 729–749, https://doi.org/10.1039/C9QM00554D.

[27] C. Xiang, M. Li, M. Zhi, A. Manivannan, N. Wu, Reduced graphene oxide/titanium dioxide composites for supercapacitor electrodes: shape and coupling effects, J. Mater. Chem. 22 (2012) 19161–19167, https://doi.org/10.1039/C2JM33177B.

[28] S.Bin Mujib, B. Vessalli, W.A. Bizzo, T. Mazon, G. Singh, Cassava- and bamboo-derived carbons with higher degree of graphitization for energy storage, Nanomater. Energy 9 (2020) 54–65, https://doi.org/10.1680/jnaen.19.00040.

[29] S. Yang, S. Wang, X. Liu, L. Li, Biomass derived interconnected hierarchical micro-meso-macro- porous carbon with ultrahigh capacitance for supercapacitor, Carbon N. Y. 147 (2019) 540–549, https://doi.org/10.1016/j.carbon.2019.03.023.

[30] K.M. Shell, D.D. Rodene, V. Amar, A. Thakkar, B. Maddipudi, S. Kumar, R. Shende, R.B. Gupta, Supercapacitor performance of corn stover-derived biocarbon produced from the solid co-products of a hydrothermal liquefaction process, Bioresour. Technol. Rep. 13 (2021) 100625, https://doi.org/10.1016/j.biteb.2021.100625.

[31] Y.X. Yang, K.K. Ge, S. ur Rehman, H. Bi, Nanocarbon-based electrode materials applied for supercapacitors, Rare Met 41 (2022) 3957–3975, https://doi.org/10.1007/s12598-022-02091-1.

[32] D. Ouyang, L. Hu, G. Wang, B. Dai, F. Yu, L. Zhang, A review of biomass-derived graphene and graphene-like carbons for electrochemical energy storage and conversion, N. Carbon Mater. 36 (2021) 350–372, https://doi.org/10.1016/s1872-5805(21)60024-0.

[33] A. Abbas, X.E. Eng, N. Ee, F. Saleem, D. Wu, W. Chen, M. Handayani, T.A. Tabish, N. Wai, T.M. Lim, Development of reduced graphene oxide from biowaste as an electrode material for vanadium redox flow battery, J. Energy Storage 41 (2021) 102848, https://doi.org/10.1016/j.est.2021.102848.

[34] T. Kongthong, C. Poochai, C. Sriprachuabwong, Journal of Science: Advanced Materials and Devices Microwave-assisted synthesis of nitrogen-doped pineapple leaf fiber- derived activated carbon with manganese dioxide nano fibers for high-performance coin- and pouch-cell supercapacitors, 7 (2022).

[35] M. Wahid, D. Puthusseri, D. Phase, S. Ogale, Enhanced capacitance retention in a supercapacitor made of carbon from sugarcane bagasse by hydrothermal pretreatment, Energy Fuels 28 (2014) 4233–4240, https://doi.org/10.1021/ef500342d.

[36] Z. Zhao, Y. Huang, W. Ren, L. Zhao, X. Li, M. Wang, Y. Lin, Natural biomass hydrogel based on cotton fibers/PVA for acid supercapacitors, ACS Appl. Energy Mater. 4 (2021) 9144–9153, https://doi.org/10.1021/acsaem.1c01404.

[37] F. Barzegar, A.A. Khaleed, F.U. Ugbo, K.O. Oyeniran, D.Y. Momodu, A. Bello, J. K. Dangbegnon, N. Manyala, Cycling and floating performance of symmetric supercapacitor derived from coconut shell biomass, AIP Adv. 6 (2016) 115306, https://doi.org/10.1063/1.4967348.

[38] K. C, T. V.R, P. S, N. Reddy, C. Hu, K. Venkatesh, S. V.C, N. N, N. K, KOH activated carbon derived from biomass-banana fibers as an efficient negative electrode in high performance asymmetric supercapacitor, J. Energy Chem. 26 (2017) 56–62, https://doi.org/10.1016/j.jechem.2016.07.003.

[39] R. Wang, P. Wang, X. Yan, J. Lang, C. Peng, Q. Xue, Promising porous carbon derived from celtuce leaves with outstanding supercapacitance and CO2 capture performance, ACS Appl. Mater. Interfaces 4 (2012) 5800–5806, https://doi.org/10.1021/am302077c.

[40] C. Long, X. Chen, L. Jiang, L. Zhi, Z. Fan, Porous layer-stacking carbon derived from in-built template in biomass for high volumetric performance supercapacitors, Nano Energy 12 (2015) 141–151, https://doi.org/10.1016/j.nanoen.2014.12.014.

[41] S.J. Ki, H. Lee, Y.-K. Park, S.-J. Kim, K.-H. An, S.-C. Jung, Assessing the electrochemical performance of a supercapacitor electrode made of copper oxide and activated carbon using liquid phase plasma, Appl. Surf. Sci. 446 (2018) 243–249, https://doi.org/10.1016/j.apsusc.2018.01.044.

[42] B. Pal, S. Yang, S. Ramesh, V. Thangadurai, R. Jose, Electrolyte selection for supercapacitive devices: a critical review, Nanoscale Adv. 1 (2019) 3807–3835, https://doi.org/10.1039/c9na00374f.

[43] J. Zhang, L. Sun, C. Liao, C. Yan, A simple route towards tubular ZnO, Chem. Commun. (2002) 262–263, https://doi.org/10.1039/B108863G.

[44] V. Sudha, G. Murugadoss, R. Thangamuthu, Structural and morphological tuning of Cu-based metal oxide nanoparticles by a facile chemical method and highly electrochemical sensing of sulphite, Sci. Rep. 11 (2021) 3413, https://doi.org/10.1038/s41598-021-82741-z.

[45] Z.Q. Li, C.J. Lu, Z.P. Xia, Y. Zhou, Z. Luo, X-ray diffraction patterns of graphite and turbostratic carbon, Carbon N. Y. 45 (2007) 1686–1695, https://doi.org/10.1016/j.carbon.2007.03.038.

[46] M.A. Pimenta, G. Dresselhaus, M.S. Dresselhaus, L.G. Cançado, A. Jorio, R. Saito, Studying disorder in graphite-based systems by Raman spectroscopy, Phys. Chem. Chem. Phys. 9 (2007) 1276–1290, https://doi.org/10.1039/B613962K.

[47] L.M. Malard, M.A. Pimenta, G. Dresselhaus, M.S. Dresselhaus, Raman spectroscopy in graphene, Phys. Rep. 473 (2009) 51–87, https://doi.org/10.1016/j.physrep.2009.02.003.

[48] Y. Song, S. Zhang, C. Zhang, Y. Yang, K. Lv, Raman spectra and microstructure of zinc oxide irradiated with swift heavy ion, Crystals 9 (2019), https://doi.org/10.3390/cryst9080395.

[49] R.F. Zhuo, H.T. Feng, Q. Liang, J.Z. Liu, J.T. Chen, D. Yan, J.J. Feng, H.J. Li, S. Cheng, B.S. Geng, X.Y. Xu, J. Wang, Z.G. Wu, P.X. Yan, G.H. Yue, Morphology-controlled synthesis, growth mechanism, optical and microwave absorption properties of ZnO nanocombs, J. Phys. D. Appl. Phys. 41 (2008), https://doi.org/10.1088/0022-3727/41/18/185405.

[50] O. Prakash, S. Kumar, P. Singh, V. Deckert, S. Chatterjee, A.K. Ghosh, R.K. Singh, Surface-enhanced Raman scattering characteristics of CuO: Mn/Ag heterojunction probed by methyl orange: effect of Mn2+ doping, J. Raman Spectrosc. 47 (2016) 813–818, https://doi.org/10.1002/jrs.4904.

[51] A.C. Ferrari, J. Robertson, Interpretation of Raman spectra of disordered and amorphous carbon, Phys. Rev. B. 61 (2000) 14095–14107, https://doi.org/10.1103/PhysRevB.61.14095.

[52] D.B. Schuepfer, F. Badaczewski, J.M. Guerra-Castro, D.M. Hofmann, C. Heiliger, B. Smarsly, P.J. Klar, Assessing the structural properties of graphitic and non-graphitic carbons by Raman spectroscopy, Carbon N. Y 161 (2020) 359–372, https://doi.org/10.1016/j.carbon.2019.12.094.

[53] N. Shimodaira, A. Masui, Raman spectroscopic investigations of activated carbon materials, J. Appl. Phys. 92 (2002) 902–909, https://doi.org/10.1063/1.1487434.

[54] A.C. Ferrari, J. Robertson, A.C. Ferrari, J. Robertson, Raman spectroscopy of amorphous, nanostructured, diamond–like carbon, and nanodiamond, Philos. Trans. R. Soc. Lond. Ser. A Math. Phys. Eng. Sci. 362 (2004) 2477–2512, https://doi.org/10.1098/rsta.2004.1452.

[55] C. Sasirekha, S. Arumugam, G. Muralidharan, Green synthesis of ZnO/carbon (ZnO/C) as an electrode material for symmetric supercapacitor devices, Appl. Surf. Sci. 449 (2018) 521–527, https://doi.org/10.1016/j.apsusc.2018.01.172.

[56] S. Zhang, N. Pan, Supercapacitors performance evaluation, Adv. Energy Mater. 5 (2015) 1401401, https://doi.org/10.1002/aenm.201401401.

[57] S. Rawat, T. Boobalan, B.B. Krishna, M. Sathish, S. Hotha, T. Bhaskar, Biochar for supercapacitor application: a comparative study, Chem. - Asian J. 17 (2022), https://doi.org/10.1002/asia.202200982.

[58] S. Suresh, H.C. Prakash, M.S. Kumar, S.K. Batabyal, Manganese-doped polyaniline electrodes as high-performance supercapacitors with superior energy density and prolonged shelf life, J. Sci. Adv. Mater. Devices 8 (2023) 100639, https://doi.org/10.1016/j.jsamd.2023.100639.

[59] M. Rajkumar, C.T. Hsu, T.H. Wu, M.G. Chen, C.C. Hu, Advanced materials for aqueous supercapacitors in the asymmetric design, Prog. Nat. Sci. Mater. Int. 25 (2015) 527–544, https://doi.org/10.1016/j.pnsc.2015.11.012.

[60] R. Anjana, P.M. Anjana, J. Alex, R. Isaac, R.S.S. Hussain, D. Sajan, Investigations on supercapacitor performance of novel ZnO-CeO2-rGO nanohybrid prepared via hydrothermal method for energy storage applications and their charge storage mechanism, Diam. Relat. Mater. 146 (2024) 111241, https://doi.org/10.1016/j.diamond.2024.111241.

[61] M. Forghani, S.W. Donne, Method comparison for deconvoluting capacitive and pseudo-capacitive contributions to electrochemical capacitor electrode behavior, J. Electrochem. Soc. 165 (2018) A664, https://doi.org/10.1149/2.0931803jes.

[62] A. Elgendy, N.M. El Basiony, F. El-Taib Heakal, A.E. Elkholy, Mesoporous Ni-Zn-Fe layered double hydroxide as an efficient binder-free electrode active material for high-performance supercapacitors, J. Power Sources 466 (2020) 228294, https://doi.org/10.1016/j.jpowsour.2020.228294.

[63] G. Nabi, A. Siddiqa, M. Tanveer, A. Nadeem, K. Shahzad Ahmad, Manganese substitution effects on structural and electrochemical performance of CoFe2O4 for promising supercapacitor electrode materials, Inorg. Chem. Commun. (2024) 112850, https://doi.org/10.1016/j.inoche.2024.112850.

[64] J.V. Paulin, S.L. Fernandes, C.F.O. Graeff, Solid-state electrochemical energy storage based on soluble melanin, Electrochem 2 (2021) 264–273, https://doi.org/10.3390/electrochem2020019.

[65] B.-A. Mei, O. Munteshari, J. Lau, B. Dunn, L. Pilon, Physical interpretations of nyquist plots for EDLC electrodes and devices, J. Phys. Chem. C. 122 (2018) 194–206, https://doi.org/10.1021/acs.jpcc.7b10582.

[66] Z.V. Saponjic, N.M. Dimitrijevic, D.M. Tiede, A.J. Goshe, X. Zuo, L.X. Chen, A. S. Barnard, P. Zapol, L. Curtiss, T. Rajh, Shaping nanometer-scale architecture through surface chemistry, Adv. Mater. 17 (2005) 965–971, https://doi.org/10.1002/adma.200401041.

[67] Y. Shao, J. Li, Y. Li, H. Wang, Q. Zhang, R.B. Kaner, Flexible quasi-solid-state planar micro-supercapacitor based on cellular graphene films, Mater. Horiz. 4 (2017) 1145–1150, https://doi.org/10.1039/C7MH00441A.

[68] X. Dong, Y. Cao, J. Wang, M.B. Chan-Park, L. Wang, W. Huang, P. Chen, Hybrid structure of zinc oxide nanorods and three dimensional graphene foam for supercapacitor and electrochemical sensor applications, RSC Adv. 2 (2012) 4364–4369, https://doi.org/10.1039/C2RA01295B.

[69] K. Chen, D. Xue, Colloidal supercapacitor electrode materials, Mater. Res. Bull. 83 (2016) 201–206, https://doi.org/10.1016/j.materresbull.2016.06.013.